Soil-expended seismic metamaterial with ultralow and wide bandgap

Yongtao Bai*[1,2], Xiaolei Li[2], Xuhong Zhou[1,2], Peng Li[3], and Michael Beer[4,5,6]

1 Research Center for Steel Structure Engineering, Chongqing University, China

2 School of Civil Engineering, Chongqing University, China

3 College of Aerospace Engineering, Nanjing University of Aeronautics and Astronautics, Nanjing 210016, China

4 Institute for Risk and Reliability, Leibniz University of Hannover, 30167 Hannover, Germany

5 Institute for Risk and Uncertainty, The University of Liverpool, Liverpool L69 7ZF, UK

6 International Joint Research Center for Resilient Infrastructure & International Joint Research Center for Engineering Reliability and Stochastic Mechanics, Tongji University, Shanghai, China

Abstract: The low-frequency wide-bandgap characteristics of the seismic metamaterial can suppress the propagation of vibrations and reduce the risk of extreme loadings such as earthquakes. The stringent requirement of lattice size extensively increasing with the cost of forming seismic metamaterial using general engineering materials. We design soil-expanded seismic metamaterial to reduce the scale restriction on artificial materials. Two types of soil-expanded lattice are created, and the bandgap characteristics for the lattice are obtained through the transfer matrix method. The propagation process for finite periodic lattice is simulated by the finite difference method in the time domain. It is found that the acceleration amplitudes in the wave propagation region are suppressed by 90% for the seismic metamaterial with rubber components. The response spectra

* E-Mail: bai.yongtao@cqu.edu.cn

further indicate that seismic metamaterials can reduce seismic risk in targeted areas.

Keywords: Vibration attenuation, Seismic metamaterial, Bandgap, Periodic structures, Soil-structure interaction, Seismic prevention.

1. Introduction

Earthquake, sudden and devastating natural disaster, has been well known for bringing huge casualties and economic losses and is still a huge challenge for all mankind [1-3]. Various theories and techniques have been developed to promote structural seismic resistance, but these measures can only protect the structure in which it is located, and earthquake-indenergy-absorbing elements can cause considerable damage under large earthquakes. These damages are often difficult to repair or even so difficult to replace that the structure can no longer be used [4,5]. The presence of these problems makes earthquakes still a huge threat to cities. Recently, the advent of phononic crystal acoustic metamaterials has allowed us to directly control the propagation of elastic waves. Seismic waves are elastic; they can also be controlled by phononic crystals, meaning that region-scale phononic crystals have the potential to enable earthquake protection for entire urban areas. Phononic crystal is an artificial acoustic metamaterial composed of periodically distributed media [6] when region-scale metamaterials are particularly designed for seismic this kind of metamaterial as seismic crystals [7] or seismic metamaterials(SMs) [8].

Seismic metamaterials consist of a series of identical lattices that prevent elastic waves in certain frequency ranges from propagating through the metamaterial. These frequency ranges are often referred to as bandgaps and are the essence of seismic metamaterials that can control the propagation of seismic waves. The realization of bandgaps is based on periodically repeating lattices. The geometry, density, and

Young’s modulus of the lattice control the location and width of the band gaps. Specially designed low-frequency bandgap seismic metamaterials can prevent seismic waves from propagating into urban areas or critical structures such as power plants and hospitals.

Over the last decade, considerable literature has grown up around the topic of surface wave attenuation by seismic metamaterials. A number of authors have considered the formation of bandgaps by periodically burying artificial structures below the ground to attenuate seismic surface waves. Pu [9, 10] analyzed surface wave attenuation by periodically cylindrical concrete piles, calculated the effect of soil stratification on bandgaps, and proposed a new method for identifying surface wave bandgaps. Zhang [11], Miniaci [12] and Amanat [13] presented seismic metamaterials with different cross-sections, they calculated the bandgaps and transmission properties of seismic metamaterials by commercial finite element software. Considering the anisotropy of the soil, Guo et al [14] combined theoretical derivation and numerical modelling to calculate the bandgaps and transmission curve of rubber-steel piles. The authors proposed a low-frequency bandgap seismic metamaterial in anisotropic soil. Using laboratory experiments, Zeng [15] and Chen [16] verified the bandgaps of two different seismic metamaterials through transmission curve. Different with mentioned above, Brûlé [17] and Kacin [18] constructed periodic holes with different distribution shapes in natural soil and verified the ability of seismic metamaterials to attenuate surface waves by amplitude distribution. In addition, some studies have shown that the periodic attachment of specially designed structures to the soil surface is also capable of forming bandgaps. By commercial finite element software, the bandgaps and transmission curve of built-up structural steel sections [19], H-fractal seismic metamaterial [20], Minkowski-like fractal seismic metamaterial [21], T-shaped seismic metamaterial [22] and Matryoshka-like seismic metamaterial [23] are well analyzed. Recently, Zeng [24] pointed out that negative Poisson's ratio materials are more conducive to the formation of low-frequency metamaterials. However, such studies remain narrow in focus dealing only with surface waves attention.

Seismic waves are divided into surface waves and body waves. Surface waves propagate only in the horizontal direction, while body waves can propagate in both the horizontal and vertical directions. There is little published data on the attention of body waves through seismic metamaterials [7,25]. As noted by Geng, one-dimensional layered seismic metamaterials can effectively attenuate body waves propagating in any direction [25]. They calculated the bandgap of a two-component layered seismic metamaterial by a theoretical method and discussed the effect of material properties on the width and location of the first-order bandgap. Geng argues that it is hard for two-component seismic metamaterials to form low-frequency bandgaps when the artificial material thickness is less than the seismic wavelength. However, they only calculated the bandgaps for shear waves. For longitudinal waves in soil, which have longer wavelengths, it is even more difficult to form bandgaps with the same lattice thickness. In addition, little is known about the transmission properties of seismic metamaterials with only finite dimensions in the aperiodic direction.

This paper discusses the case of attention of body waves by one-dimensional seismic metamaterial. Two kind of one-dimensional seismic metamaterial to reduce the thickness of artificial material are presented, both of them expanded lattice by soil. There are two primary aims of this study: 1. To investigate the influence of soil thickness to bandgaps. 2. To ascertain transmission properties of this kind of seismic metamaterial. Firstly, the effect of soil thickness and artificial material thickness on the bandgap of both longitudinal wave and shear wave by transfer matrix method is analysed. Subsequently, the finite difference method in time domain (FDTD) is used to simulate the transmission properties of one-dimensional seismic metamaterials. Finally, the transmission properties of layered seismic metamaterials with finite size in aperiodic direction are simulated by 2D FDTD considering the practical situation.

2. Model and Bandgaps of soil-expanded lattice

2.1 The model of soil-expanded lattices

Many researchers have utilized soil as a matrix to form two- or three-dimensional seismic metamaterials. However, one-dimensional layered seismic metamaterials have no difference between matrix and scatterer, and the lattice contains only artificial material. As a result, such a lattice cannot have dimensions comparable to seismic wavelengths. Although it can somewhat control transverse waves, it isn't easy to control longitudinal waves. To make the lattice size of the one-dimensional layered seismic metamaterial comparable to the seismic wavelength, we propose two soil-expanded lattices, as shown in Fig. 1.

Fig. 1(a) shows a schematic diagram of the protection of a target building by one-dimensional seismic metamaterial. As shown in Fig. 1(a), the seismic metamaterial is placed in front of the target building. As shown in Fig. 1(b) and Fig. 1(c), two types of soil-expanded lattices are illustrated. The red dashed box marked the lattice. The lattice shown in Fig. 1(b) consists of concrete and soil (CS lattice), while the lattice shown in Figure 1(c) consists of a concrete layer wrapped in rubber in front and behind and soil (CRS lattice). Compared to Fig. 1(b), the CRS lattice in Fig. 1(c) contains rubber, which is more conducive to forming band gaps through the local resonance mechanism.

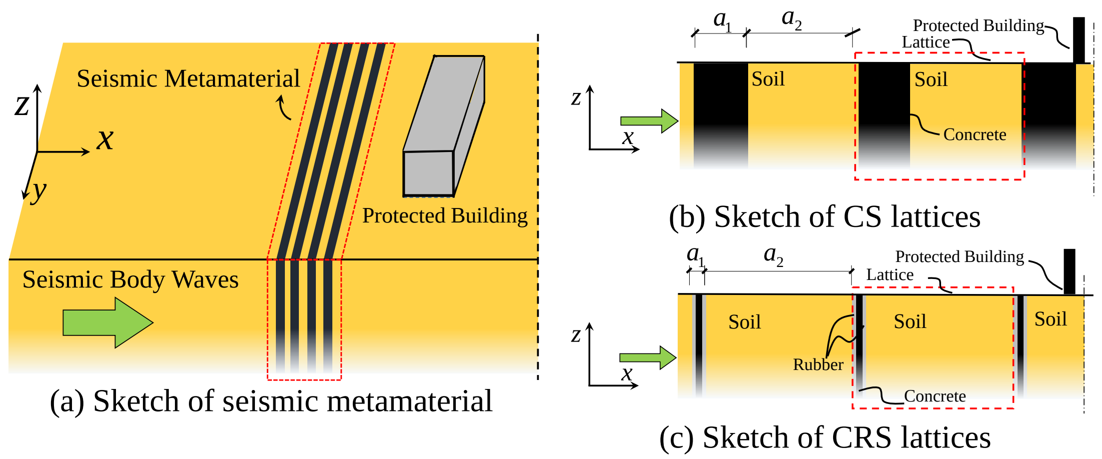

Fig. 1 Soil-expanded lattices

It is worth noting that both soil-expanded lattices make the soil an integral part of the lattice. So in both soil-expanded lattices, increasing the thickness of the soil increases the lattice size. As the seismic metamaterial is buried in the soil, controlling the soil thickness is easy to realize, that is, maintaining the burial distance between each concrete layer.

2.2 bandgaps of soil-expanded lattice

Eqn. 1 shows the equation for the propagation of an elastic wave in a one-dimensional metamaterial.

$$\frac{\partial^2 U(x,t)}{\partial t^2} = \frac{1}{C} \cdot \frac{\partial^2 U(x,t)}{\partial x^2} \quad (1)$$

where $U(x,t)$ is the displacement field in the computational domain, and C is the elastic wave velocity. In infinitely repeating one-dimensional layered metamaterials, the displacement fields at the ends of the lattice satisfy the Bloch period condition shown in Eqn. 2.

$$U(x+a) = e^{-ika} \cdot U(x) \quad (2)$$

where $U(x)$ is the displacement at the left end of the lattice, and $U(x+a)$ is the displacement at the right end of the lattice. i is an imaginary number and k is the wave number, a is the length of lattice. The eigenfrequency analysis of each wave number k of the lattice shown in Fig. 1(b) and Fig. 1(c) using the transfer matrix method enables the dispersion equation for the field expansion lattice to be obtained, as shown in Eqn. 3.

$$2\cos\left[k(a_1+a_2)\right]=\cos\left(\frac{\omega a_1}{C_1}\right)\cos\left(\frac{\omega a_2}{C_2}\right)-\frac{C_1\mu_2}{\mu_1 C_2}\cdot\sin(\frac{\omega a_1}{C_1})\sin(\frac{\omega a_2}{C_2})-\frac{C_2}{\omega\cdot\mu_2}\cdot\left(\frac{\mu_1\cdot\omega\cdot\sin(\frac{\omega a_1}{C_1})\sin(\frac{\omega a_2}{C_2})}{C_1}-\frac{\omega\cdot\mu_2\cos\left(\frac{\omega a_1}{C_1}\right)\cos\left(\frac{\omega a_2}{C_2}\right)}{C_2}\right) \tag{3-a}$$

$$2\cos\left[k(a_1+a_2)\right]=\cos\left(\frac{\omega a_1}{C_1}\right)\cos\left(\frac{\omega a_2}{C_2}\right)-\frac{(\lambda_2+2\mu_2)C_1}{(\lambda_1+2\mu_1)C_2}\cdot\sin(\frac{\omega a_1}{C_1})\sin(\frac{\omega a_2}{C_2})-\frac{C_2}{\omega\cdot(\lambda_2+2\mu_2)}\cdot\left(\frac{(\lambda_1+2\mu_1)\cdot\omega\cdot\sin(\frac{\omega a_1}{C_1})\sin(\frac{\omega a_2}{C_2})}{C_1}-\frac{\omega\cdot(\lambda_2+2\mu_2)\cos\left(\frac{\omega a_1}{C_1}\right)\cos\left(\frac{\omega a_2}{C_2}\right)}{C_2}\right) \tag{3-b}$$

$$\begin{aligned}
&2\cos\left[k(a_1+a_2)\right]=\frac{1}{C_2\cdot C_3{}^2\cdot C_4\cdot\mu_2\cdot\mu_3^2\cdot\mu_4}\cdot\{\\
&\cos^2(\frac{\omega a_1}{C_3})\cdot[-\sin(\frac{\omega a_1}{C_2})\sin(\frac{a_2\omega}{C_4})\cdot(C_3^2\mu_4^2+C_4^2\mu_3^2)\cdot(C_2^2\mu_3^2+C_3^2\mu_2^2)+4\cos(\frac{\omega a_1}{C_2})\cos(a_2\frac{\omega a_1}{C_4})C_2C_3^2C_4\cdot\mu_2\cdot\mu_3^2\cdot\mu_4]-\\
&2C_3\mu_3\sin(\frac{\omega a_1}{C_3})\cos(\frac{\omega a_1}{C_3})\cdot[C_2\mu_2\cos(\frac{\omega a_1}{C_2})\sin(a_2\frac{\omega a_1}{C_4})(C_3^2\mu_4^2+C_4^2\mu_3^2)+C_4\mu_4\sin(\frac{\omega a_1}{C_2})\cos(a_2\frac{\omega a_1}{C_4})(C_2^2\mu_3^2+C_3^2\mu_2^2)]+\\
&\sin(\frac{\omega a_1}{C_2})\sin(\frac{\omega a_2}{C_4})(C_2^2C_4^2\mu_3^4+C_3^4\mu_2^2\mu_4^2)-\\
&2\cos(\frac{\omega a_1}{C_2})\cos(\frac{\omega a_2}{C_4})C_2\cdot C_3^2\cdot C_4\cdot\mu_2\cdot\mu_3^2\cdot\mu_4\}
\end{aligned} \tag{3-c}$$

$$\begin{aligned}
&2\cos\left[k(a_1+a_2)\right]=\frac{1}{C_2\cdot C_3{}^2\cdot C_4\cdot(\lambda_2+2\mu_2)\cdot(\lambda_3+2\mu_3)^2\cdot(\lambda_4+2\mu_4)}\cdot\{\\
&\cos^2(\frac{\omega a_1}{C_3})\cdot[-\sin(\frac{\omega a_1}{C_2})\sin(\frac{a_2\omega}{C_4})\cdot(C_3^2(\lambda_4+2\mu_4)^2+C_4^2(\lambda_3+2\mu_3)^2)\cdot(C_2^2(\lambda_3+2\mu_3)^2+C_3^2(\lambda_2+2\mu_2)^2)+4\cos(\frac{\omega a_1}{C_2})\cos(a_2\frac{\omega a_1}{C_4})C_2C_3^2C_4\cdot(\lambda_2+2\mu_2)\cdot(\lambda_3+2\mu_3)^2\cdot(\lambda_4+2\mu_4)]-\\
&2C_3(\lambda_3+2\mu_3)\sin(\frac{\omega a_1}{C_3})\cos(\frac{\omega a_1}{C_3})\cdot[C_2(\lambda_2+2\mu_2)\cos(\frac{\omega a_1}{C_2})\sin(a_2\frac{\omega a_1}{C_4})(C_3^2(\lambda_4+2\mu_4)^2+C_4^2(\lambda_3+2\mu_3)^2)+C_4(\lambda_4+2\mu_4)^2\sin(\frac{\omega a_1}{C_2})\cos(a_2\frac{\omega a_1}{C_4})(C_2^2(\lambda_3+2\mu_3)^2+C_3^2(\lambda_2+2\mu_2)^2)]+\\
&\sin(\frac{\omega a_1}{C_2})\sin(\frac{\omega a_2}{C_4})(C_2^2C_4^2(\lambda_3+2\mu_3)^4+C_3^4(\lambda_2+2\mu_2)^2(\lambda_3+2\mu_3)^2)-\\
&2\cos(\frac{\omega a_1}{C_2})\cos(\frac{\omega a_2}{C_4})C_2\cdot C_3^2\cdot C_4\cdot(\lambda_2+2\mu_2)\cdot(\lambda_3+2\mu_3)^2\cdot(\lambda_4+2\mu_4)\}
\end{aligned} \tag{3-d}$$

where a_1 is the thickness of the concrete layer of the CS lattice in Eqn.(3-a) and Eqn. (3-b). a_1 is the thickness of the concrete layer of the CRS lattice including the outer rubber layer in Eqn. (3-c) and Eqn. (3-d). And a_2 is the thickness of the soil in Eqn. (3-a), Eqn. (3-b), Eqn. (3-c) and Eqn. (3-d). a_1 , a_2 are geometrical parameters, and they are all illustrated in Fig. 1. In Eqn. 3, μ_n and λ_n are the Lame constants, and C_n is wave velocity of the Nth layer. k is wave number and ω is angular frequency. Eqn. (3-a) and Eqn. (3-b) describes the dispersion equation for the CS lattice, Eqn. (3-c) and Eqn. (3-d) describes the dispersion equation for the CRS lattice. The detailed analysis of Bloch's boundary conditions and the derivation of Eqn. 3 can be found in Supplementary Material S1 and literature [26-28].

When the wave number k in Eqn. 3 is specified, a number of eigenfrequency f that satisfy the equation can be calculated. Since the lattice is periodically repeated, the dispersion curve is obtained by calculating only the wave number k within the first Brillouin zone($k \in \left(-\dfrac{\pi}{2a}, \dfrac{\pi}{2a}\right)$), where a is the length of the lattice. When there is no corresponding wave number k in a section of frequency, these frequency sections are called bandgaps. As we can see, there is more than one bandgap. The upper and lower boundaries of bandgaps determine the location and width of the bandgaps. If an elastic wave has only frequencies within the bandgaps, such an elastic wave cannot propagate through seismic metamaterials. Seismic waves are ultra-low frequency elastic waves, the main frequency component of which is 0-15 Hz. Therefore, seismic metamaterials should have a bandgap that is sufficiently low frequency and as wide as possible. The bandgap with the smallest lower bound mark is bandgap 1st, and as the frequency rises, the other bandgaps are 2nd, 3rd, and so on. By taking $k = \pi / (2a)$ into Eqn. 3, we can obtain the upper and lower bound frequencies for the odd bandgaps. Bringing $k = 0$ into Eqn.3 gives the upper and lower bounds of the bandgap for order bandgaps.

Since the lower bound of bandgap number one has the lowest frequency, we take $k = \pi / 2 \cdot a$ into account Eqn. 3 and calculate odd bandgaps. Note that the dispersion equations for the CS and CRS lattices have the artificial material layer thickness parameter and the soil thickness parameter, which can influence the upper and lower bound of the band gap. Therefore, the frequency f is calculated using the artificial material layer thickness parameter a_1 and the soil thickness parameter a_2 as variables, as shown in Fig. 2. Fig. 2(a) shows the distribution of the upper and lower boundaries of the odd-numbered bandgap for the CS lattice in both modes. The vertical coordinate is the frequency, the axis a_1 represents the concrete thickness, and the axis a_2 represents the soil layer thickness. Fig. 2(b) shows the distribution of the upper and lower boundaries of the odd-numbered bandgap of the CRS lattice for both modes. The vertical coordinate is the frequency f, the axis a_1 represents the total thickness of the rubber and concrete layers, and the axis a_2 represents the soil thickness. The material data are shown in Tab. 1, where V_p and V_s is the wave velocity of the longitudinal wave and shear wave. ρ is the density of the material, μ and λ are the Lame coefficient of the material.

Table 1 Material property in CS and CRS lattice

Material	V_p (m/s)	V_s (m/s)	ρ (g/cm³)	μ	λ
C30 Concrete	3800	2820	2.36	9.4×10^{9}	1.82×10^{10}
Soil	1500	210	1.93	8.49×10^{7}	2.12×10^{9}
Rubber	571	45	1.3	2.67×10^{6}	4.18×10^{8}

Fig. 2 shows that the upper and lower boundaries of the odd-numbered bandgaps corresponding to different layer thicknesses. Both lattices can reduce the lower boundary of the bandgap by adding concrete and soil thickness. This may be due to the fact that increasing the concrete layer thickness is equivalent to increasing the resonator mass of the local resonance mechanism and reducing the band gap position. The CRS lattice is covered with softer rubber than soil, and the same thickness of concrete makes it easier for the local resonance mechanism to form, requiring less concrete thickness. However, the increased thickness of the artificial material layer increases the cost of the seismic metamaterial. Fig. 2(b)(d) shows the results of the analysis of the longitudinal wave mode, where we consider the value of 30m for the CS lattice and 10m for the CRS lattice.

Another trend in the bandgap in Fig. 2 is that the upper and lower boundary spacing of bandgap number one becomes smaller as the soil thickness increases, which means that the bandgap width decreases. There are two reasons for this phenomenon: on the one hand, increasing soil thickness allows for a significant increase in lattice size, which facilitates the acquisition of low-frequency band gaps. On the other hand, when the thickness of the soil increases infinitely, the seismic metamaterial will converge infinitely to the natural soil. However, natural soils do not have any bandgap, which makes the distance between the upper and lower boundaries of the bandgap decrease with increasing soil thickness.

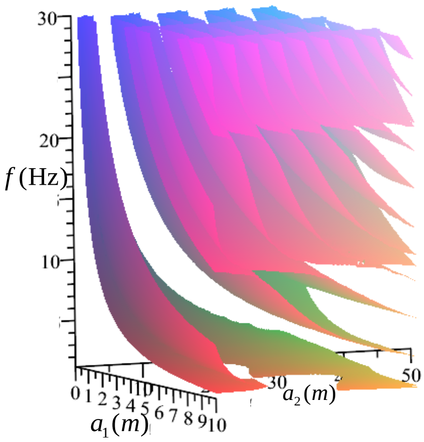

(a) CS lattice bandgaps in shear wave

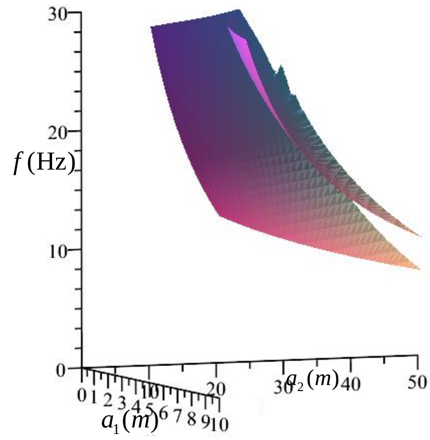

(b) CS lattice bandgaps in longitudinal wave

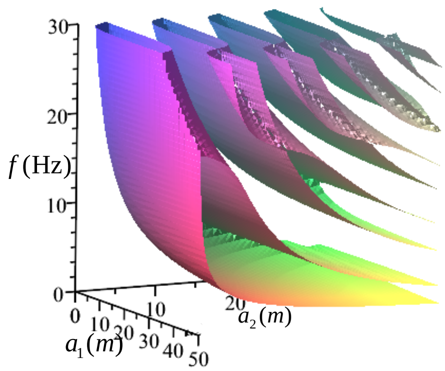

(c) CRS lattice bandgaps in shear wave

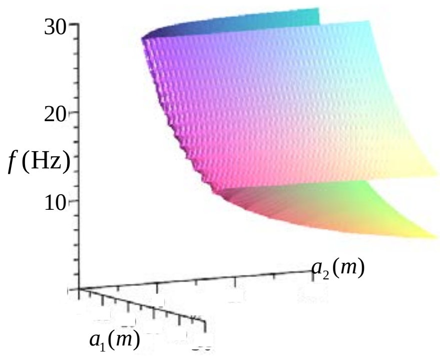

(d) CRS lattice bandgaps in longitudinal wave

Fig. 2 3D view of the bandgaps

To find a reasonable soil thickness, we take the given a_1 and $k = \pi/2 \cdot a$ into Eqn. 3, get the upper and lower bounds for the odd-numbered and even-numbered bandgaps, respectively, as shown in Fig. 3.

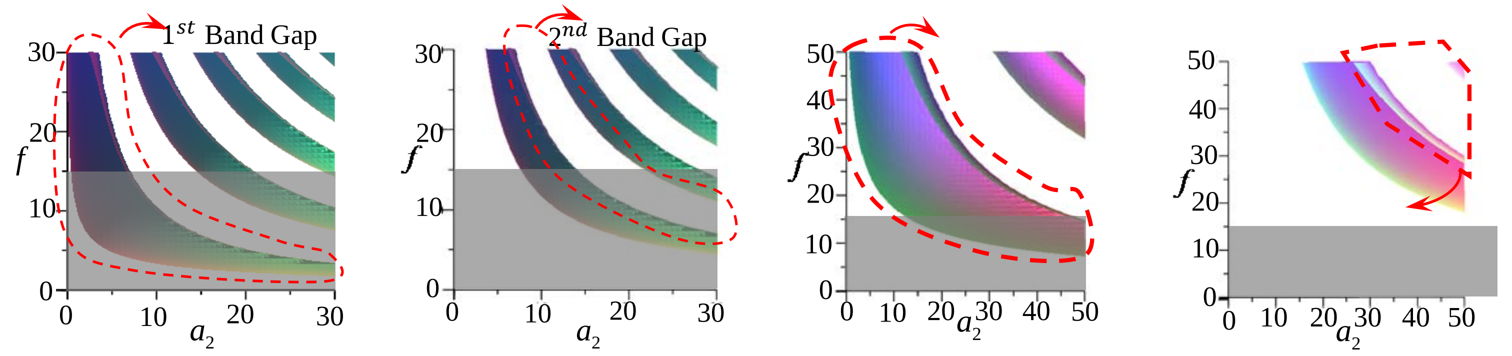

(a) CSs lattices in shear wave of odd bandgap

(b) CS lattices in shear wave of even bandgap

(c) CS lattices in longitudinal wave of odd bandgap

(d) CS lattices in longitudinal wave of even bandgap

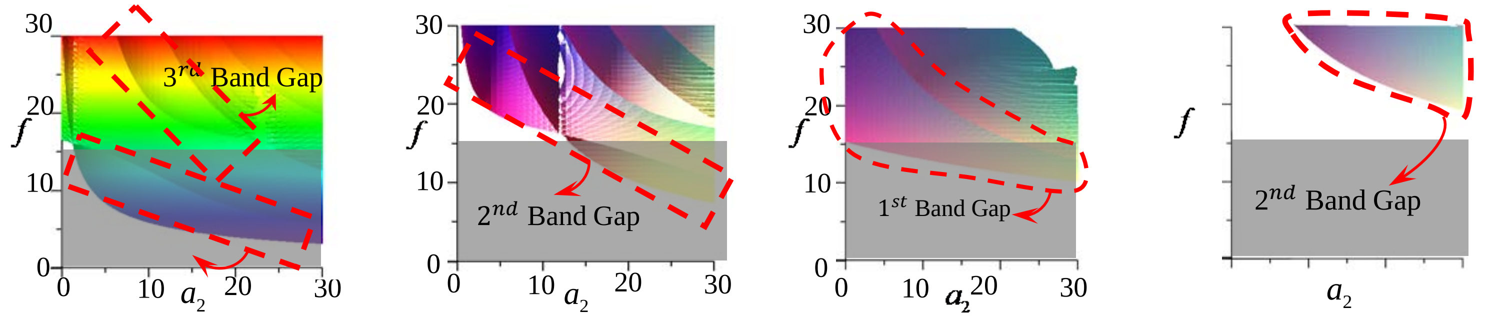

(e) CRS lattices in shear wave of odd bandgap

(f) CRS lattices in shear wave of even bandgap

(g) CRS lattices in longitudinal wave of odd bandgap

(h) CRS lattices in longitudinal wave of even bandgap

Fig. 3 Variation of bandgap with the thickness of soil

The upper and lower boundaries of the bandgap are circled with a red dash line in Fig. 3, while the grey rectangle represents the dominant frequency of the seismic wave between 0 and 15 Hz. When the red dashed box intersects the grey part of the diagram, the soil thickness is such that a valid bandgap can be formed. For example, Fig. 3(a)(b) the complete bandgap of CS lattice in shear wave model. The 1st bandgap are circled with red dash line, and has the intersect with grey part when a_2 is less than 1m. However, Fig. 3(c)(d) shows that the 1st bandgap intersect with grey part when a_2 more than 10m. For more valid bandgaps in longitudinal wave, the value of a_2 could be 50m. As the value of a_2 is more than 50m, the intersection of red wireframe and gray part gets narrower. So the value of a_2 should be 50m. Likely, we can get the soil thickness of CRS lattice. Tab. 2 shows the size of two lattices.

Table2 Size of two lattices

Lattice	a_1 (m)	a_2 (m)	a (m)
CS	30	50	80
CRS	10	30	40

Taking the thickness shown in Tab. 2 to Eqn.3, the Fig. 4 shows the dispersion curves for the CS and CRS lattice. The grey part in Fig. 4 is the bandgap. The CS and CRS lattices can form bandgaps within 0-15Hz in both modes.

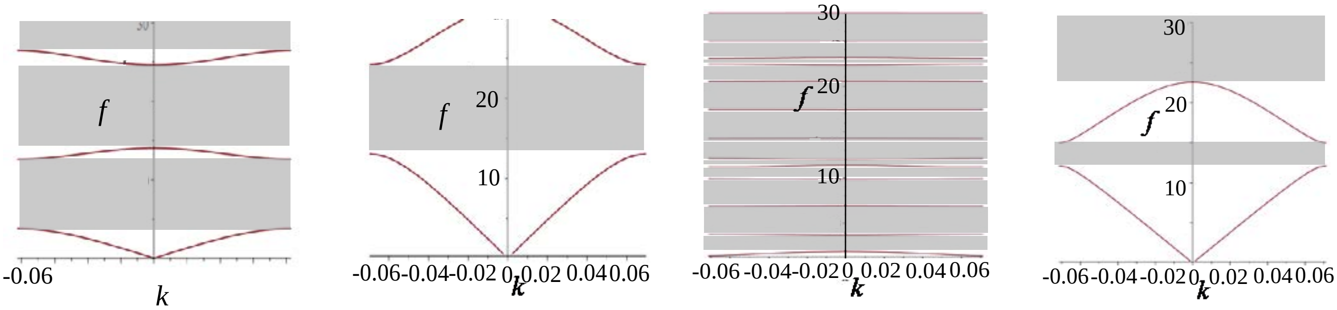

(a) CS-shear-bandgap (b) CS-longitudinal-bandgap (c) CRS-shear-bandgap (d) CRS-longitudinal-bandgap

Fig. 4 Bandgaps for various seismic metamaterial

3. Numerical simulation of soil-expanded lattice

The time-domain finite-difference method of acceleration loading is used to simulate the propagation of seismic waves through seismic metamaterials. This numerical method improves the standard time-domain finite-difference method and allows for convenient statistics on the computational domain's maximum acceleration and maximum displacement. The numerical calculation methods are described in Supplementary Material S2 and can also be found in the literature [29-31].

When the seismic metamaterial in Fig. 1(a) has infinite dimensions in the y-direction and seismic waves cannot pass the seismic metamaterial, the computational domain can be reduced to one dimension. Fig. 5 shows the one-dimensional computational domain. The PML absorption boundary is set at both ends of the computational domain, and the source is 50 m from the left-end boundary. The time history of point S1 and point S2 and the distribution of maximum acceleration and maximum displacement are recorded during the computation.

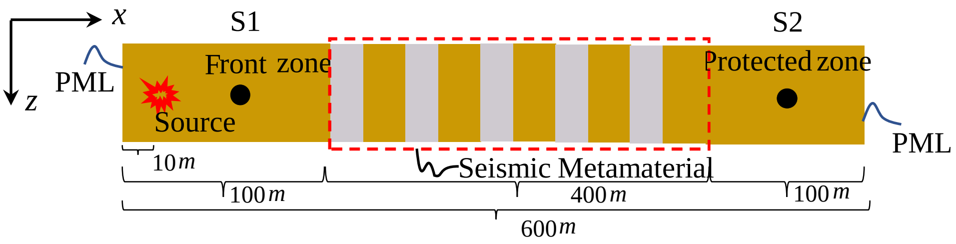

(a) seismic metamaterial by CS lattice

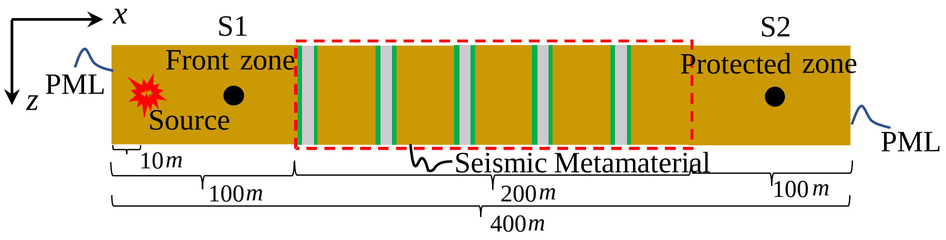

(b) seismic metamaterial by CRS lattice

Fig. 5 Seismic metamaterial with infinite length in y direction

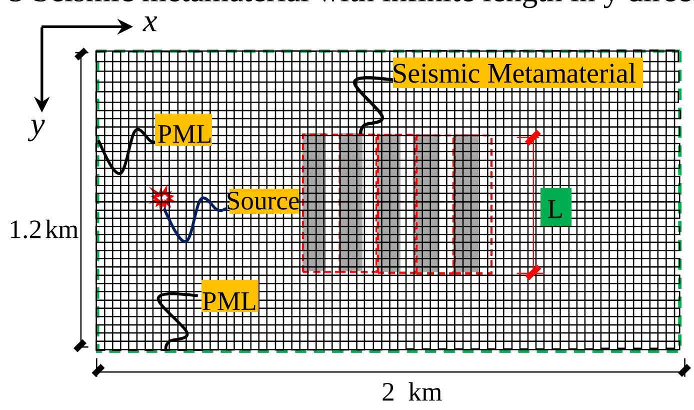

Fig. 6 Seismic metamaterial with finite length in y direction

When the seismic metamaterial in Fig. 1(a) has only a finite size in the y-direction, there is a possibility that the seismic wave will go around to the back of the seismic metamaterial during propagation, as shown in Fig. 6. The computational domain is a square area of 1.2km×2.0km. The four sides of the square are set with PML absorption boundaries. The length of seismic metamaterial in the y-direction is 600m.

3.1 1D numerical analysis

We used seismic wave data from the PEER website, El-Centro Array #9, from the earthquake of Imperial Valley-05. this seismic wave has a rich low frequency component. Fig. 7 shows the time history and spectrum of the seismic wave.

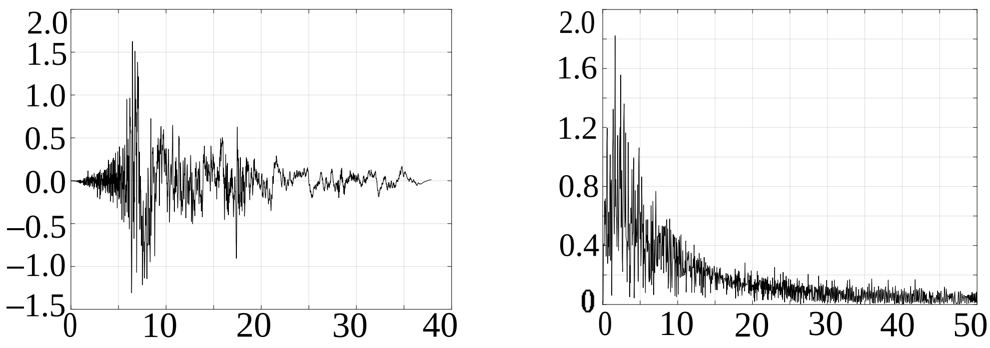

(

（a）Station recording time history b）Station recording spectrum

Fig. 7 The source schedule of seismic wave

Considering shear waves, the seismic waves were analyzed using the finite difference method in the time domain through the one-dimensional computational domain shown in Fig. 5, and the maximum displacement and acceleration distributions within all computational domains were counted, as shown in Fig. 8.

Fig. 8 shows the distribution of the maximum acceleration and displacement of the seismic wave through the 1D computational domain. The "Uniform" and "SMs" labels mark the natural soil and the seismic metamaterial, respectively, as shown by the blue and red curves in Fig. 8. "F zone" and "P zone" mark the front and back of the seismic metamaterial. Fig. 8(a)(b) shows the CS seismic metamaterial compared to natural soil, and Fig. 8(c)(d) shows the CRS seismic metamaterial compared to natural soil.

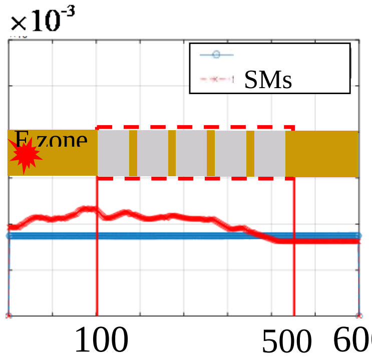

(a) Peak Displacement of CS seismic metamaterial

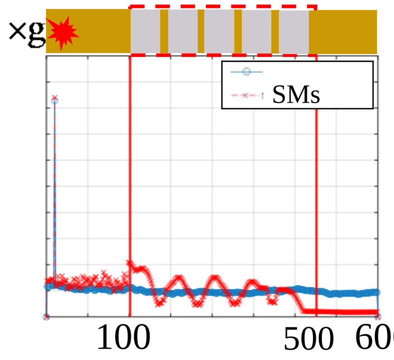

(b) Peak Acceleration of CRS seismic metamaterial

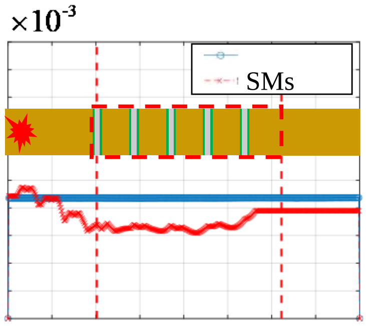

(c) Peak Displacement of CRS seismic metamaterial

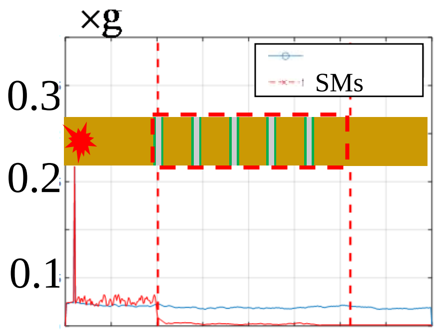

(d) Peak Acceleration of CRS seismic metamaterial

Fig. 8 Max displacement and acceleration

Firstly, both lattices effectively attenuate seismic waves, as seen from the red curve in Fig. 8, which is lower in the 'P zone' than the blue curve. It can be seen that the red curve in Fig. 8(b)(d) is significantly lower than the blue curve. Both lattices are better at attenuating acceleration than displacement. As acceleration is an important indicator of earthquake engineering, it can directly respond to the magnitude of the seismic forces in a structure. Therefore, installing seismic metamaterials in front of the protected building can effectively reduce the seismic forces on the structure.

Secondly, the attenuation process of seismic waves differs significantly between the two lattices. The maximum acceleration within the CS seismic metamaterial in Fig. 8(b) produces a peak at the concrete layer, and the peak decreases as the lattice increases. The peak is probably due to the high shear force where the concrete is located, and the acceleration required to balance the shear force increases accordingly, creating a peak.

In contrast, the maximum acceleration within the CRS seismic metamaterial decays directly to near zero in the first lattice, and there is no peak in the acceleration within the seismic metamaterial. The wave impedance of the concrete layer is much higher than that of the rubber layer, resulting in a direct reflection of the elastic wave so that the maximum acceleration in the CRS seismic metamaterial is more evenly distributed and very close to 0. The red curve in the "F zone" section of Fig. 8(d) is higher than the blue curve, illustrating the reflection phenomenon.

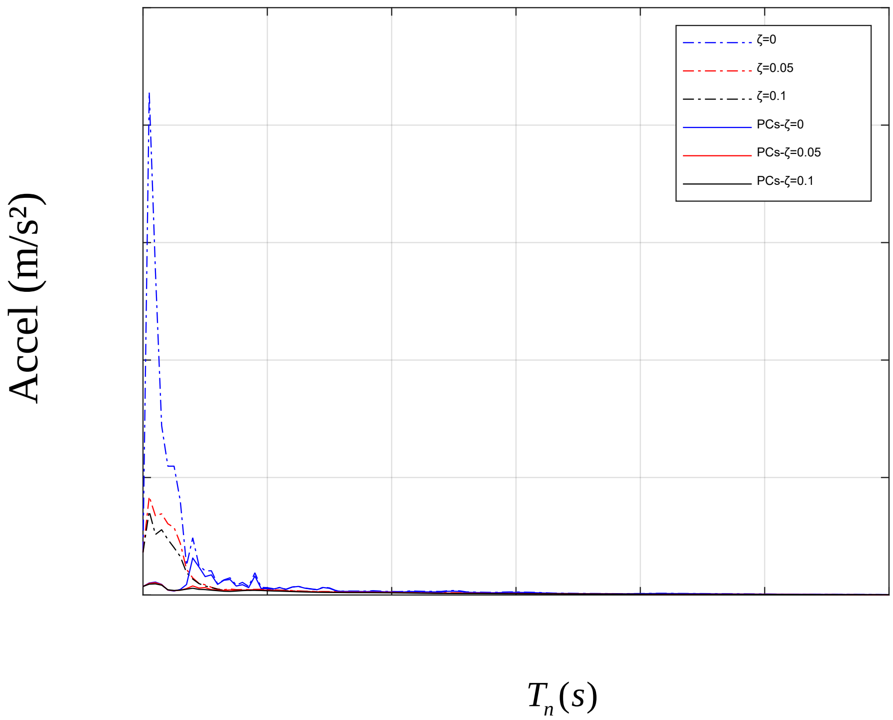

(a) CR lattice acceleration response spectrum

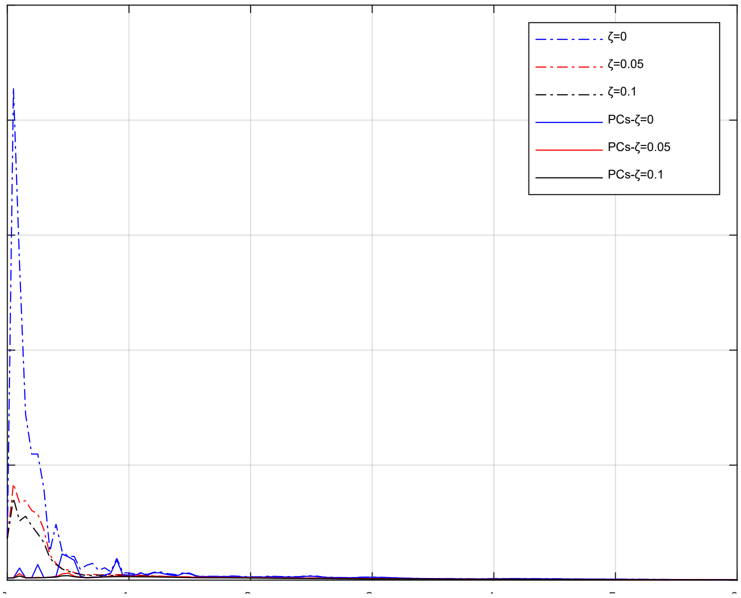

$T_n(s)$

(b) CRS lattice acceleration response spectrum

Fig. 9 response spectrum of seismic metamaterial

The dashed line in Fig. 9 is the response spectrum for the time course recorded at monitoring point S1, and the solid line is the response spectrum for the table time course recorded at monitoring point S2. The different colored curves represent the additional damping of the response spectra. It can be seen that the peak of the response spectrum at point S2 is significantly lower than the peak of the response spectrum at point S1, irrespective of the damping level. Buildings in the 'P zone' are at substantially lower seismic risk than those in the 'F zone.' Both seismic metamaterials significantly reduce the seismic hazard in the protected area.

3.2 Lattice Equivalence Phenomenon

In contrast to higher-dimensional seismic metamaterial, the scatterer and matrix within the lattice of a 1D seismic metamaterial do not strictly distinguish between each other, which are merely different layers. When we introduce such soil-expanded lattice, the lattice just is a finite number of layers inserted periodically in the soil. The lattice positions indicated by the red boxes in Fig. 1 are only one case, and Fig. 10 shows a fully equivalent lattice schematic to the red boxes.

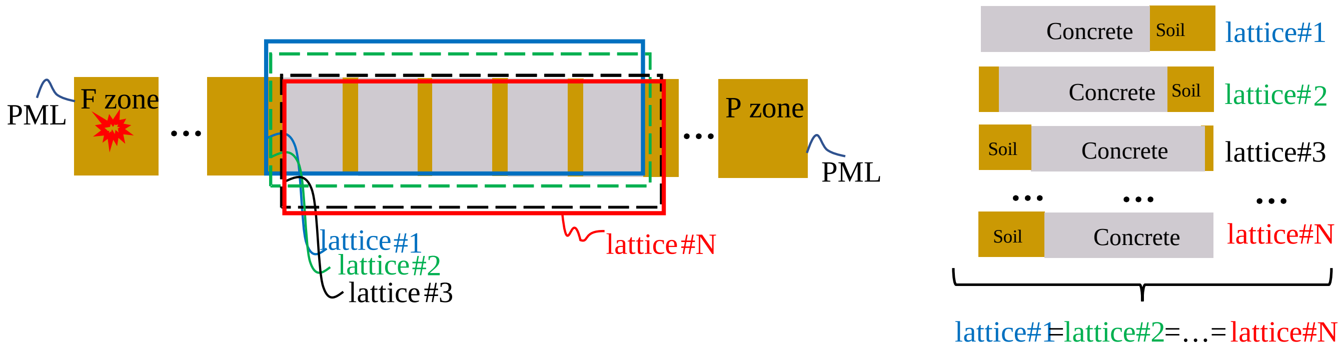

(a) CS lattice equivalence

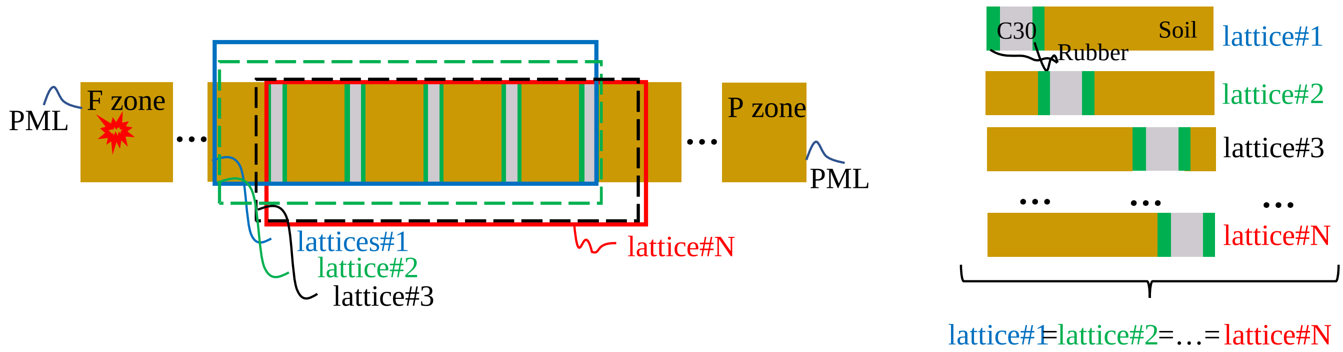

(b) CRS lattice equivalence

Fig. 10 Phenomenon of lattice equivalence

In Fig. 10(a) and Fig. 10(b), the red wireframe and other frames are equivalent lattices, and the difference between them is mainly the difference in lattice form. In the figure's red wireframe and other color wireframes, any wireframes of equal length can be completely equivalent lattices. This lattice equivalence makes it impossible for elastic waves to identify a complete CS or CRS lattice. At both ends of the seismic metamaterial, the part that acts as a soil infill will still have significant fluctuations and will not get shock absorption because it is a soil infill.

3.3 2D numerical analysis

For the CRS lattice, when the seismic metamaterial has finite dimensions in the y-direction, we use a two-dimensional time domain finite difference method to simulate the propagation of elastic waves in the seismic metamaterial. We choose a harmonic wave located within the bandgaps as the seismic source, and Eqn. 5 shows the time expression.

$$a(t) = 0.01 \times \left[0.5 \cdot \sin(2\pi \cdot 8t) + 0.3 \cdot \sin(2\pi \cdot 18t) + 0.2 \cdot \sin(2\pi \cdot 23t) \right] \quad (5)$$

Fig. 11 gives the results of numerical calculations of seismic metamaterials with a finite length in the y-direction. On the left are the results for natural soil, labeled 'uniform.' The seismic metamaterials simulation results are on the right, labeled "SMs." The red boxes mark the areas of enhanced vibration due to reflections, and the green boxes mark the areas of seismic protection provided by the seismic metamaterials. When the length of the seismic metamaterial is limited in the y-direction, the area of protection provided by the seismic metamaterial is a trapezoid.

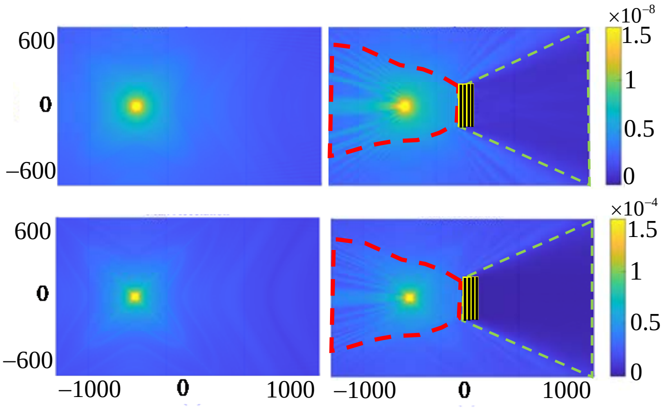

Fig. 11The attenuation and amplification zone of finite length without rotation

4. Conclusion

In this paper, two kinds of soil-expanded seismic metamaterial models were proposed. Then, the transfer matrix method investigated the effect of layer thickness on the bandgaps of the CS lattice and CRS lattice. Subsequently, the propagation of elastic waves through the seismic metamaterial is simulated using the time domain finite difference method. The way in which the seismic metamaterials work is discussed by comparing the maximum acceleration and maximum displacement distributions of the seismic metamaterials and the natural soil in the one-dimensional computational domain. By analyzing the response spectrum in front of the seismic metamaterial and the response spectrum behind the seismic metamaterial, it is demonstrated that the two seismic metamaterials can enhance the seismic safety of the target building. The range of seismic safety zones formed by the seismic metamaterials is found by comparing the maximum acceleration and maximum displacement distributions of the seismic metamaterials with the natural soil in the two-dimensional calculation domain.

(1) Both CRS lattice and CS lattice could form lower bandgaps by soil expanded mechanism. While the thickness of the soil layer can lower the position of the bandgap, it can also lead to a reduction in the width of the band gap. A reasonable soil layer thickness should take into account an appropriate reduction of the band gap position and not an excessive narrowing of the bandgap width.

(2) The CS lattice attenuates seismic waves slowly and more strongly with a higher number of lattices, while the CRS lattice reflects them directly, independent of the number of lattices.

(3) The distribution of the maximum displacement and the distribution of the maximum acceleration indicates that the wave cannot distinguish lattice position due to the lattice equivalence phenomenon.

(4) Compared with natural soil, the peak value of the response spectrum in the protected area after the addition of lattice decreased, among which the peak value of the response spectrum in the s-wave mode decreased by 90 %.

(5) Seismic metamaterials of finite length can form trapezoidal seismic safety zones. The vibration-strengthening zone due to reflections is also trapezoidal.

5. Acknowledgement

This study was partially supported by the National Key R&D Program of China under Grant No. 2022YFB2602700, the National Natural Science Fund for Excellent Young Scientists Fund Program, Scientific Research Fund of the Institute of Engineering Mechanics, China Earthquake Administration (2020EEEVL0413), and the Support Plan for Returned Overseas Scholars of Chongqing (cx2020022).

Reference

[1] Harris, R.A. “Large earthquakes and creeping faults.” Rev. Geophys, 2017. 55: 169-198.

[2] Li J., Peng, T., Xu, Y. “Damage investigation of girder bridges under the Wenchuan earthquake and corresponding seismic design recommendations.” Earthquake Eng Eng Vibr, 2008. 7(4): 337-44.

[3] Nguyen, W., Trono, W., Panagiotou, M. “Seismic response of a rocking bridge column using a precast hybrid fiber-reinforced concrete (HyFRC) tube.” Compos Struct, 2017. 174: 252-62.

[4] Ellingwood, B.R. “Risk-informed condition assessment of civil infrastructure: state of practice and research issues.” Structure and Infrastructure Engineering, 2005. 1(1): 7-18.

[5] Frangopol, D.M. “Life-cycle performance, management, and optimization of structural systems under uncertainty:accomplishments and challenges.” Structure and Infrastructure Engineering, 2011. 7(6): 389–413.

[6] Wang, P., L. Lu, and K. Bertoldi, Topological Phononic Crystals with One-Way Elastic Edge Waves. Physical Review Letters, 2015. 115(10).

[7] Alagoz, B.B. and S. Alagoz, Towards Earthquake Shields: A Numerical Investigation of Earthquake Shielding with Seismic Crystals. Open Journal of Acoustics, 2011. 01(03): p. 63-69.

[8] Huang, J.K. and Z.F. Shi, Attenuation zones of periodic pile barriers and its application in vibration reduction for plane waves. Journal of Sound and Vibration, 2013. 332(19): p. 4423-4439.

[9] Pu, X.B. and Z.F. Shi, Surface-wave attenuation by periodic pile barriers in layered soils. Construction and Building Materials, 2018. 180: p. 177-187.

[10] Pu, X.B. and Z.F. Shi. “A novel method for identifying surface waves in periodic structures. ”Soil Dynamics and Earthquake Engineering, 2017. 98: p. 67-71.

[11] Zhang, K., et al., Seismic metamaterials with cross-like and square steel sections for low-frequency wide band gaps. Engineering Structures, 2021. 232.

[12] Miniaci, M., et al., Large scale mechanical metamaterials as seismic shields. New Journal of Physics, 2016. 18.

[13] Amanat, S., et al., Analytical and numerical investigation of finite and infinite periodic lattices for mitigation of seismic waves in layered grounds. International Journal of Engineering Science, 2022. 173.

[14] Guo, D.K. and T.Y. Chen, Seismic metamaterials for energy attenuation of shear horizontal waves in transversely isotropic media. Materials Today Communications, 2021. 28.

[15] Zeng, Y., et al., A broadband seismic metamaterial plate with simple structure and easy realization. Journal of Applied Physics, 2019. 125(22).

[16] Chen, Y.Y., et al., Harnessing multi-layered soil to design seismic metamaterials with ultralow frequency band gaps. Materials & Design, 2019. 175.

[17] Brule, S., et al., Experiments on Seismic Metamaterials: Molding Surface Waves. Physical Review Letters, 2014. 112(13).

[18] Kacin, S., et al., Experimental verification of phononic crystal based on square arrays of cylindrical holes against seismic vibrations in full-scale systems: modeling, sensing and signal processing of seismic vibrations. Archive of Applied Mechanics, 2022. 92(1): p. 309-323.

[19] Muhammad, C.W. Lim, and J.N. Reddy, Built-up structural steel sections as seismic metamaterials for surface wave attenuation with low frequency wide bandgap in layered soil medium. Engineering Structures, 2019. 188: p. 440-451.

[20] Du, Q.J., et al., H-fractal seismic metamaterial with broadband low-frequency bandgaps. Journal of Physics D-Applied Physics, 2018. 51(10).

[21] Fan, L., et al., Minkowski-like fractal seismic metamaterial with wide low-frequency band gaps on single and layered soil. Journal of Physics D-Applied Physics, 2022. 55(49).

[22] Zeng, Y., et al., Broadband inverted T-shaped seismic metamaterial. Materials & Design, 2021. 208.

[23] Zeng, Y., et al., A Matryoshka-like seismic metamaterial with wide band-gap characteristics. International Journal of Solids and Structures, 2020. 185: p. 334-341.

[24] Huang, T.T., et al., Based on auxetic foam: A novel type of seismic metamaterial for Lamb waves. Engineering Structures, 2021. 246.

[25] Geng, Q., S.Y. Zhu, and K.P. Chong, Issues in design of one-dimensional metamaterials for seismic protection. Soil Dynamics and Earthquake Engineering, 2018. 107: p. 264-278.

[26] Filonov, V. et al. “Transfer matrix method for analysis of flow thermohydraulic characteristics with extremely nonlinear behavior of thermophysical properties using channel approach.” International Journal of Heat and Mass Transfer, 2022.187: 122531.

[27] Dell, A. et al. “The use of the transfer matrix method to predict the effective fluid properties of acoustical systems.” Applied Acoustics, 2021.182: 108259.

[28] Shahsavari, H. et al. “Analysis of wave propagation through functionally graded porous cylindrical structures considering the transfer matrix method.” Thin-Walled Structures, 2021.159: 107212.

[29] Shahmohamadi, B. et al. “Analysis of dipole plasma antenna using kinetic method and FDTD numerical approach.” AEU - International Journal of Electronics and Communications, 2022. 145: 154066.

[30] Li, X. et al. “FDTD simulation on transmittance of silica microsphere thin films with varying embedding in an optical adhesive.” Optik, 2021.241: 166997.

[31] Meng, H. et al. “Modelling of anisotropic beam for rotating composite wind turbine blade by using finite-difference time-domain (FDTD) method.” Renewable Energy, 2020. 162: 2361-2379.

[32] Agha, W. and Umamaheswari, N. “Analytical study of irregular reinforced concrete building with shear wall and dual Framed-Shear wall system by using Equivalent Static and Response Spectrum Method.” Materials Today: Proceedings, 2021. 43: 2232-2241.

[33] Jayaram, N. et al. “A Computationally Efficient Ground-Motion Selection Algorithm for Matching a Target Response Spectrum Mean and Variance.” Earthquake Spectra, 2011. 27(3): 797-815.

[34] Yun, J., and Han, J, “Evaluation of soil spring methods for response spectrum analysis of pile-supported structures via dynamic centrifuge tests.” Soil Dynamics and Earthquake Engineering, 2021. 141: 106537.

Supplement Material S1

The one-dimensional fluctuation equation is as in Eqn. S1-1.

$$\frac{\partial^2 U}{\partial t^2} = \frac{1}{C} \cdot \frac{\partial^2 U}{\partial x^2} \tag{S1-1}$$

where C is the wave velocity, which can be determined as longitudinal wave velocity by $c_p = \sqrt{(2\mu + \lambda)/\rho}$ or shear wave velocity $c_s = \sqrt{\mu/\rho}$, corresponding to the shear wave propagation equation and the longitudinal wave propagation equation. Assuming that the model satisfies infinite repetition in the period domain, the computational model satisfies the Bonn-Kamen boundary condition, as shown in Fig. 1.

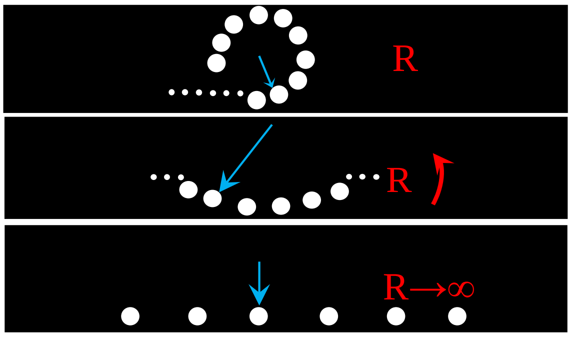

Fig. S1 Bonn-Kamen Boundary

One-dimensional seismic metamaterials possess the Bonn-Kamen boundary condition shown in Fig. S1. It is assumed that the blue arrows represent the field functions $\Phi(x)$ at the coordinates x, and the white origin represents the position of the lattice. When the number of lattices is limited, the crystal is assumed to take the form of a ring of radius R. Assuming that there are n_1 lattices in the ring, the field function after one lattice satisfies equation S1-2.

$$\left|\Phi(x)\right|^2 = \left|\Phi(x+a)\right|^2 \qquad \text{(S1-2)}$$

where a is the lattice length. Eqn. S1-2 is equivalent to Eqn. S1-3.

$$\Phi(x)=q_1 \cdot \Phi(x+a) \qquad \text{(S1-3)}$$

After n_1 lattice, the field function returns to the coordinate x and satisfies the Eqn. S1-4

$$\Phi(x)=q_1^n \cdot \Phi(x) \qquad \text{(S1-4)}$$

Obviously, $q_1^n=1$, and $q_1=\sqrt[n]{1}$, and q_1 can be replaced by Eqn. S1-5.

$$q_1=e^{i\cdot 2\pi \cdot \frac{n}{n_1}} \qquad \text{(S1-5)}$$

As the radius R of the ring crystal increases, the number of lattices n_1 increases accordingly, as shown in Figure S1-(b). As R increases to infinity, the crystal can be considered to be in the form of a straight chain, and for each lattice passed, the form of the field function will satisfy Eqn. S1-6.

$$\Phi\left(x\right)=e^{i\cdot\frac{2\pi n}{N}\cdot\frac{\left(x+a\right)}{a}}\Phi\left(x+a\right)=e^{i\cdot k\cdot a}\Phi\left(x+a\right) \qquad \text{(S1-6)}$$

where , $k=\frac{2\pi\cdot n}{N}$, N is the total number of lattices. Eqn. S1-6 is the Bonn-Kamen boundary condition.

Supplement Material S2

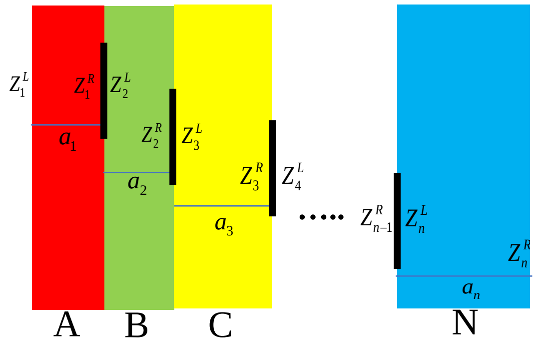

Fig. S1 Transfer matrix calculation process

Fig. S2 shows a one-dimensional lattice, with A, B, C...N being the different material layers. Two adjacent layers should satisfy displacement continuity and shear stress continuity. The nth layer displacement and shear stress are shown in Eqn. S2-1 and Eqn. S2-2 respectively.

$$u_n(x_n) = A_n \sin\left(\frac{\omega}{C_{sn}} x_n\right) + B_n \cos\left(\frac{\omega}{C_{sn}} x_n\right) \tag{S2-1}$$

$$\tau_n(x_n) = \frac{\mu_n \omega}{C_{sn}}\left[A_n \cos\left(\frac{\omega}{C_{sn}} x_n\right) - B_n \sin\left(\frac{\omega}{C_{sn}} x_n\right)\right] \tag{S2-2}$$

where x_n is the local coordinate of the nth level. A_n and B_n is the coefficient to be determined. C_{sn} is the shear wave velocity. Let $Z_n(x_n)$ be the state function, as shown in Eqn. S2-3.

$$Z_n(x_n) = H_n(x_n) \cdot \Psi(x_n) \tag{S2-3}$$

where $H_n(x_n)$ is the state quantity, as shown in Eqn. S2-4. $\Psi(x_n)$ is the coefficient like vector to be determined, as shown in Eqn. S2-5.

$$H_n(x_n)=\begin{bmatrix} \sin\left(\dfrac{\omega}{C_{sn}}x_n\right) & \cos\left(\dfrac{\omega}{C_{sn}}x_n\right) \\ \dfrac{\mu_n\omega}{C_{sn}}\cos\left(\dfrac{\omega}{C_{sn}}x_n\right) & -\dfrac{\mu_n\omega}{C_{sn}}\sin\left(\dfrac{\omega}{C_{sn}}x_n\right) \end{bmatrix} \tag{S2-4}$$

$$\Psi=\begin{bmatrix} A_n & B_n \end{bmatrix}^T \tag{S2-5}$$

The state function on the left side of the nth level is shown in Equation S2-6. The state function on the right-hand side of the nth level is shown in Eqn. S2-7.

$$Z_n^L = H_n(0)\cdot\Psi_n \tag{S2-6}$$

$$Z_n^R = H_n(a_n)\cdot\Psi_n \tag{S2-7}$$

The relationship between Z_n^L and Z_n^R is shown in Eqn. S2-8.

$$Z_n^R = H_n(a_n)\left[H_n(0)\right]^{-1}\cdot Z_n^L \tag{S2-8}$$

Due to the continuous displacement between two adjacent layers, there is

$$Z_{n+1}^L = Z_n^R \tag{S2-8}$$

Thus, the state function from the leftmost to the rightmost part of the lattice satisfies Eqn. S2-9.

$$Z_{\mathrm{n}}^R = \left(H_n(a_n)\left[H_n(0)\right]^{-1}\cdot H_{n-1}(a_{n-1})\left[H_{n-1}(0)\right]^{-1}...H_1(a_1)\left[H_1(0)\right]^{-1}\right)Z_1^L \tag{S2-9}$$

And the state function is one that satisfies the Bonn-Kamen boundary condition, as shown in Eqn. S2-10.

$$Z_{\mathrm{n}}^R = e^{ika}\cdot Z_1^L \tag{S2-10}$$

The characteristic equation for lattice is shown in Eqn. S2-11.

$$0=\left(\mathbf{H}_n(a_n)\left[\mathbf{H}_n(0)\right]^{-1}\cdot...\mathbf{H}_1(a_1)\left[\mathbf{H}_1(0)\right]^{-1}-e^{ika}\mathbf{I}\right)Z_1^L \tag{S2-10}$$

By solving this characteristic equation, the corresponding dispersion curve of the lattice can be obtained.

Supplement Material S3

The one-dimensional fluctuation equation is shown in Eqn. S3-1. The two-dimensional z-mode fluctuation equation is shown in Eqn. S3-2.

$$\frac{\partial^2 U(x,t)}{\partial t^2} = \frac{1}{C} \cdot \frac{\partial^2 U(x,t)}{\partial x^2} \tag{S3-1}$$

$$\rho \frac{\partial^2 U_z(x,y,t)}{\partial t^2} = \mu \frac{\partial^2 U_z(x,y,t)}{\partial x^2} + \mu \frac{\partial^2 U_z(x,y,t)}{\partial y^2} \tag{S3-2}$$

Where, C_s and C_p are the transverse and longitudinal wave velocities of the material, ρ and μ and λ are the density and Lame coefficients of the material, respectively. $U(x,t)$ and $U(x,y,t)$ are the displacement fields in the 1D elastic wave equation and the 2D elastic wave equation.

Using the Taylor expansion to approximate the partial derivative term, the central difference form partial derivative term is shown in Eqn. S3-3 and Eqn. S3-4.

$$D_{xx}U(x,t) = \frac{\partial^2 U(x,t)}{\partial x^2} = \frac{U(x+\Delta x,t) + U(x-\Delta x,t) - 2\cdot U(x,t)}{\Delta x^2} \tag{S3-3}$$

$$D_{tt}U(x,t) = \frac{\partial^2 U(x,t)}{\partial t^2} = \frac{U(x,t+\Delta t) + U(x,t-\Delta t) - 2\cdot U(x,t)}{\Delta t^2} \tag{S3-4}$$

When a reasonable spatial step Δx and time step Δt are chosen, the entire computational domain is discretized into a spatial grid and a temporal grid. The spatial grid consists of two multidimensional arrays representing the displacements in the computational domain and the accelerations in the computational domain: the accelerations and displacements at positions i, j at the kth instant are denoted as $U_{i,j}^{k}$ and $a_{i,j}^{k}$.

In the numerical simulation of elastic waves in the computational domain, it is necessary to calculate from the moment 0 at the beginning of the time interval to the end of the time interval. The central difference format of the time-domain finite-difference method is to extrapolate the displacement of the computational domain at the next moment from the displacement at the current moment and the historical displacement point by point. At the time t_0, the acceleration at a point in the computational domain is $a_{i,j}^{k}$. At the time $t_0+\Delta t$, the computational domain is excited by an external force and the acceleration of the entire computational domain is denoted as $a_{i,j}^{k+1}$. In the above equation, the acceleration layer $a_{i,j}^{k}$ at the moment of t_0 should be calculated from the displacement layer $U_{i,j}^{k}$ as shown in Eqn. S3-5.

$$a_i^k = \frac{U_{i+1}^k + U_{i-1}^k - 2U_i^k}{\Delta t^2} \qquad \text{(S3-5)}$$

When the computational domain is affected by an external force at time t_0, the acceleration distribution a_i^{k+1} of the whole computational domain , which consists of the acceleration of the whole domain at time t_0 and the acceleration of the affected domain after the external force, is shown in Eqn. S3-6.

$$a_i^k = {a_{0i}}^k + {a_{pi}}^k \qquad \text{(S3-6)}$$

Eqn. S3-6 is the value of the acceleration layer at the moment t_0 after the specified acceleration has been loaded. Based on the acceleration distribution in the calculation domain of Eqn. S3-6, the displacement $U_{i,j}^{k+1}$ at the next moment can be back-calculated , as shown in Eqn. S3-7.

$$U_{i,j}^{k+1} = \Delta t^2 \cdot a_{i,j}^k + 2U_{i,j}^k - U_{i,j}^{k-1} \qquad \text{(S3-7)}$$

The acceleration and displacement layers are interconverted as shown in Fig. S3.

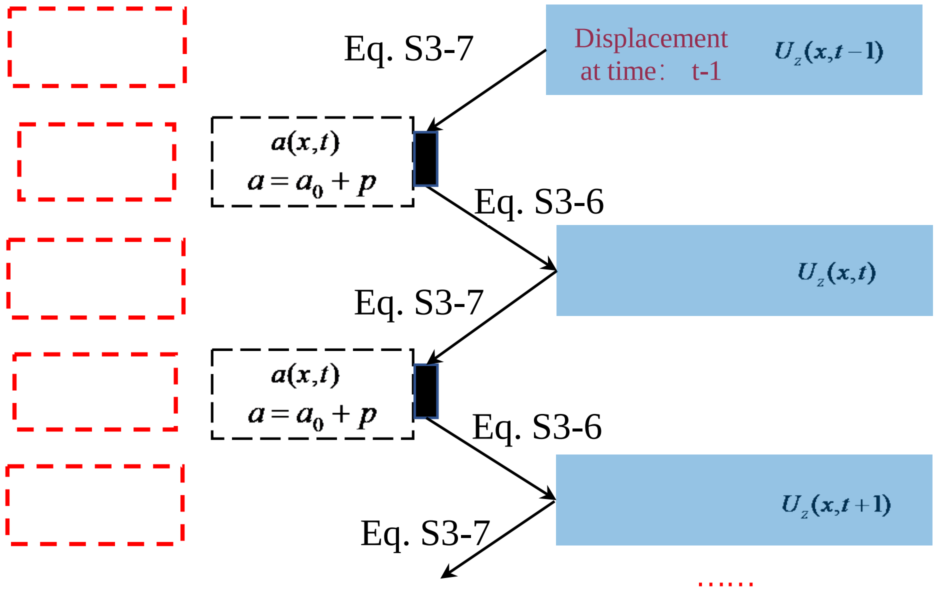

Fig. S3 Acceleration layer loading method